Chapter 6

Hydrogen binding sites in potassium intercalated graphite

6.1 Introduction

Hydrogen adsorption in KC_{24} has a relatively flat isosteric heat of adsorption (see Fig. 4.2).
A relevant question is whether this behavior can be traced to the presence of a narrow
distribution of nearly-homogeneous adsorption sites in the KC_{24} host structure. Due to
the exceptionally large incoherent cross-section of hydrogen, inelastic-incoherent-neutron
scattering (IINS) can be used effectively as a local structural probe for the adsorbed H_2
molecules. Phonon and rotational energy levels of the adsorbed H_2 molecules can both be
determined from IINS spectra and compared with calculated values. In this chapter, IINS
spectra of the $KC_{24}(H_2)_x$ are measured over a low energy range (0–2.5 meV), an intermediate
energy range (5–45 meV), and a high energy range (35–100 meV). We investigate whether
the one-dimensional hindered rotor model can successfully describe peak positions in the
low and high energy ranges. In the intermediate energy range, we attempt to describe the
rich spectral features in terms of multi-excitations of phonon and rotational energy levels.
We also assess the significance of rotational-translation coupling on the dynamics of the
$KC_{24}(H_2)_x$ system. Finally, the ground state potential energy surface of the theoretical

$KC_{28}(H_2)_1$ system is mapped from first-principles calculations, and energy levels of phonon and rotational modes are estimated.

6.2 Background

6.2.1 Rotational energy levels of the free hydrogen molecule

The free hydrogen molecule can be modeled as a rigid quantum rotor, which is well-known textbook example [110]. The eigenfunctions for the rigid rotor are the spherical harmonics $Y_l^m(\theta, \phi)$, where l is the principal angular momentum quantum number and m has the allowed values $\{0, \pm1, \pm2, \ldots \pm l\}$. The quantized energy levels for the rigid rotor are

$$E_{l,m} = l\,(l+1)\,B_{\mathrm{rot}}. \tag{6.1}$$

The energy levels are $(2l+1)$-fold degenerate in quantum number m. For the H_2 molecule, the rotational constant is equal to

$$B_{\mathrm{rot}} = \frac{\hbar}{4\pi\mu d^2} = 7.35\,\mathrm{meV}, \tag{6.2}$$

where $\mu = 0.5$ is the reduced mass, and $d = 74.6\,\mathrm{pm}$ is the H_2 bond length. This model is appropriate for a free H_2 molecule in a spherically symmetric potential or in a vacuum.

6.2.2 Ortho- and para-hydrogen

The nuclear spin and rotational degrees of freedom of the H_2 molecule are coupled due to the quantum mechanical symmetry restrictions. Since individual hydrogen nuclei are indistinguishable fermions, the total H_2 wavefunction must be antisymmetric under exchange.

The total wavefunction is constructed from both the rotational and nuclear spin wavefunctions, $\psi_{\text{total}} = Y_l^m(\theta, \phi)\psi_{\text{spin}}$. The symmetry of the rotational wavefunction under exchange can be written as $Y_l^m(\pi - \theta, \phi + \pi) = (-1)^l Y_l^m(\theta, \phi)$, which means that even values of l correspond to symmetric wavefunctions while odd values of l correspond to antisymmetric wavefunctions. The symmetric nuclear spin wavefunction (called *ortho*-hydrogen, or o-H_2) corresponds to the triplet state with total spin 1. The antisymmetric nuclear spin state (called *para*-hydrogen, or p-H_2) corresponds to the singlet state with total spin 0. In order for ψ_{total} to be anti-symmetric, even rotational states $l = 0, 2, 4, \ldots$ must be paired with the antisymmetric nuclear spin state (*para*-H_2). Similarly, the odd rotational states $l = 1, 3, 5, \ldots$ must be paired with the symmetric nuclear spin state (*ortho*-H_2). Normal hydrogen contains a 3:1 mixture of *ortho*- and *para*-hydrogen at room temperature.

6.2.3 One-dimensional hindered diatomic rotor

For an H_2 molecule in an anisotropic potential, Eq. 6.1 no longer describes the rotational energy levels. The simplest case is the one-dimensional hindered rotor model [52, 53]. The Hamiltonian for an H_2 molecule in this potential is given by

$$\hat{H} = \frac{\hat{L}^2}{2I} + \frac{V_2}{2}\left(1 - \cos 2\theta\right), \tag{6.3}$$

where V_2 is the potential energy barrier height, $\hat{L}$ is the angular momentum operator, I is the moment of inertia, and θ is the angle that the molecular axis makes with the z-axis. This one-dimensional Schrödinger equation is solved by diagonalizing the Hamiltonian matrix. After expanding the rotational potential with a spherical harmonics basis set, the
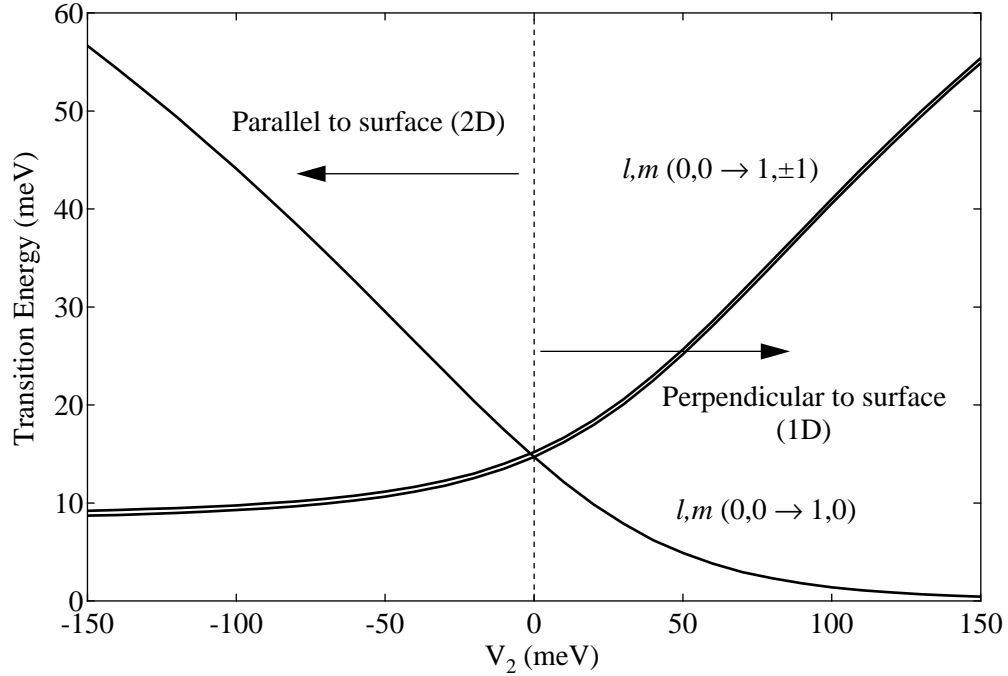
Figure 6.1: One-dimensional hindered rotor model. Rotational energy level transitions for an H_2 molecule from an $l, m(0,0)$ initial state to the first two excited states. Plotted as a function of the barrier height parameter V_2. The degenerate $l, m(1, +1)$ and $l, m(1, -1)$ states are offset slightly for clarity.

Hamiltonian matrix elements are written

$$H_{l',m',l,m} = l(l+1)B_{\text{rot}}\delta_{l',l}\delta_{m',m} + \langle Y_{l'}^{m'}|\tfrac{V_2}{2}(1 - \cos 2\theta)|Y_l^m\rangle. \tag{6.4}$$

When V_2 is positive, the H_2 molecule aligns perpendicular to the surface (1D case), and when V_2 is negative, the molecule prefers to align parallel to surface (2D case). One effect of an anisotropic potential is a lifting of the degeneracy of rotational energy levels. This is illustrated in Fig. 6.1, which plots the rotational energy level transitions from a $l, m(0,0)$ initial state as a function of V_2. The energy levels of $l, m(1, \pm 1)$ are still degenerate, but the $l, m(1,0)$ level is not. This model predicts that the single $l(0 \to 1)$ transition of free H_2 will be split into two peaks when the molecule is placed in a one-dimensional rotational potential energy well.
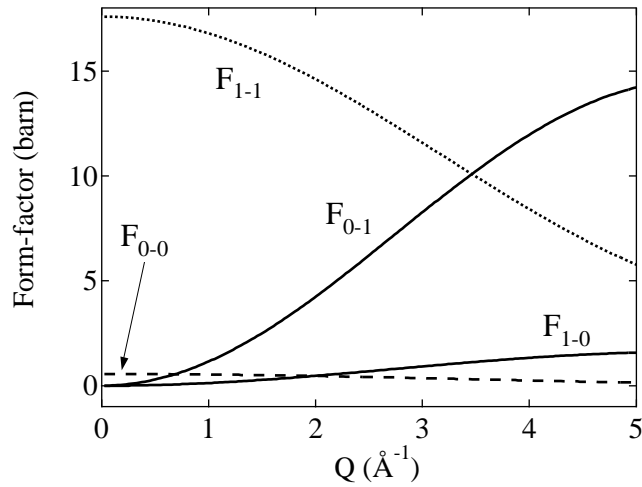
Figure 6.2: Molecular form factors for pure rotational transitions of the H_2 molecule, plotted as a function of momentum transfer. Only the transitions for the ground and first excited state are plotted.

6.2.4 Scattering law for rotational transitions of molecular hydrogen

Neutrons interact strongly with the H_2 molecule by a spin-flip transition. By flipping the nuclear spin state from paired to unpaired (or visa versa), the neutron thereby induces a transition in the H_2 rotational level. The spin of the neutron $(= \pm 1/2)$ must flip sign in this scattering event. For example, the $l(0 \to 1)$ transition has the following mechanism,

$$(\uparrow\downarrow)_{H_2}^{l=0} + (\uparrow)_n^{E_i} \xrightarrow{\sigma_{inc}} (\uparrow\uparrow)_{H_2}^{l=1} + (\downarrow)_n^{E_f}, \tag{6.5}$$

where the neutron energy loss is given by $\Delta E_{0-1} = E_i - E_f$. The double differential neutron scattering cross-section for a pure rotational transition of free H_2 has been calculated by Young and Koppel [111]. The basic idea is to use Fermi's "golden rule" to calculate the matrix element for a transition in which one or more more quantum numbers of the scatterer are changed and an equivalent amount of energy is transferred to the neutron. It is assumed that vibrations and rotations of the H_2 molecule are not coupled and that the molecule is in

the ground vibrational state. For a transition between the initial and final rotational levels l and l', the double differential scattering cross-section is expressed as

$$\frac{\mathrm{d}^2\sigma}{\mathrm{d}\Omega\mathrm{d}E} = \frac{k}{k_0}F_{l-l'}(Q)\exp(-2W)\delta(E - E_{l'} + E_l), \tag{6.6}$$

where k and k_0 are the magnitudes of the final and initial neutron wavevectors, W is the Debye-Waller factor, $F_{l-l'}(Q)$ is the molecular form factor, and the delta function enforces conservation of energy. Based on the Young-Koppel model, the molecular form factors are given by

$$F_{0-0} = 4b_\mathrm{c}^2 j_0^2\,(Qd/2) \tag{6.7}$$

$$F_{0-1} = 12b_\mathrm{inc}^2 j_1^2\,(Qd/2) \tag{6.8}$$

$$F_{1-0} = \tfrac{4}{3}b_\mathrm{inc}^2 j_1^2\,(Qd/2) \tag{6.9}$$

$$F_{1-1} = 4\left(b_\mathrm{c}^2 + \tfrac{2}{3}b_\mathrm{inc}^2\right)\left[2j_2^2\,(Qd/2) + j_0^2\,(Qd/2)\right], \tag{6.10}$$

where b_c and b_inc are the coherent and incoherent scattering lengths, d is the H_2 bond length, and j_i is the ith order spherical Bessel functions of the first kind. These molecular form-factors are plotted in Fig. 6.2. An important feature of this analysis is that the $l(0 \rightarrow 1)$ transition (and also the $l(1 \rightarrow 1)$ non-transition) is weighted by the large incoherent scattering length. However, the $l(0 \rightarrow 2)$ transition (and $l(0 \rightarrow 0)$ non-transition) is weighted by the negligibly small coherent scattering length. This means that the IINS spectrum of pure H_2 will contain a large peak at $14.7\,\mathrm{meV}$ for the $l(0 \rightarrow 1)$ transition. Further, for scattering events in which the rotational level is unchanged (e.g., pure phonon excitation), scattering from p-H_2 is negligibly small compared to o-H_2 since they are weighted by b_c

and b_{inc} respectively. However, if the transition of p-H_2 consists of a one-phonon + one-rotational multi-excitation, then the scattering cross-section will still contain the large b_{inc} factor. Therefore, the strict selection rules for rotational transitions of molecular hydrogen can be useful in interpreting the features of the IINS spectrum.

Coupling between rotational level and nuclear spin states is absent in the HD molecule since the two nuclei are distinguishable. The rotational constant for HD is equal to $B_{\mathrm{rot}} = 5.54\,\mathrm{meV}$, which means that the $l(0 \to 1)$ transition is shifted down in energy by a factor of three-fourths compared to H_2. The D_2 molecule obeys Bose statistics in which the $l = 0, 2, 4, \ldots$ states correspond to *ortho*-deuterium and the $l = 1, 3, 5, \ldots$ states correspond to *para*-deuterium. The rotational constant for D_2 is $B_{\mathrm{rot}} = 3.70\,\mathrm{meV}$, meaning that the $l(0 \to 1)$ transition is shifted by a factor of one-half compared to H_2.

6.3   Experimental methods

Inelastic neutron scattering experiments on the $KC_{24}(H_2)_x$ system were performed using the FANS instrument at NCNR [80], an indirect geometry spectrometer described in Sec. 3.2.4. Sample synthesis, handling and setup were the same as described in Sec. 5.3. The mass of KC_{24} used for this experiment was $2.935\,\mathrm{g}$. A cylindrical aluminum sample can was used without an annular insert, resulting in a larger sample thickness and consequently a significant amount of multiple scattering. Due to the lack of Q-resolution on the FANS instrument, and the qualitative nature of the measurements, this was considered acceptable. The FANS instrument contains two types of focusing monochromators bracketed between two Söller collimators of 20 inch divergence. The PG(002) monochromator can measure energy transfers of $5\,\mathrm{meV}$ to $45\,\mathrm{meV}$, while the Cu(220) monochromator can measure energy transfers of $35\,\mathrm{meV}$ to $100\,\mathrm{meV}$. It is necessary to correct the spectra for a fast-background,

caused by neutrons reaching the detector with incident energies higher than the filter cut-off limit. This fast-background contribution is easily determined by placing a cadmium shield between the sample can and the detector bank and measuring the neutron counts. Furthermore, the PG(002) monochromator suffers from some $\lambda/2$ contamination (due to higher order Bragg reflections), which can create spurious peaks at energies of $E/4$ if there is strong scattering from the sample at high energies. These features are sharper than the resolution, and can easily be identified.

To simplify interpretation of the FANS spectra, p-H$_2$ was used instead of normal H$_2$. The p-H$_2$ was prepared from normal H$_2$ by holding liquid hydrogen in a sample cell with a paramagnetic catalyst at about 10 K for at least 72 h prior to the experiment. To dispense the prepared p-H$_2$, the temperature of the holding cell was slowly increased until a specific vapor pressure was reached. In this manner, small aliquots of p-H$_2$ were introduced to the KC$_{24}$ sample until the desired loading was reached. Background measurements on bare KC$_{24}$ were first performed, followed by measurements on several KC$_{24}(p$H$_2)_x$ compositions. Data were also collected on KC$_{24}$(HD)$_{0.5}$ and KC$_{24}$(D$_2)_{0.5}$ compositions. Hydrogen was loaded at 60 K, and the sample was allowed to equilibrate for at least 20 min before lowering to base temperature. All spectra were collected at 4 K. To isolate scattering from the adsorbed H$_2$, background scattering from bare KC$_{24}$ was subtracted and the fast background was also subtracted.

Low energy-transfer measurements were performed on the DCS spectrometer. The setup was identical to that described in Sec. 5.3 in reference to the quasielastic measurements, with the exception of the incident neutron wavelength. For the current inelastic measurements, the DCS spectrometer was operated in low resolution mode with an incident neutron wavelength of 4.8 Å, a chopper speed ratio setting of 2/3, and a minimum sample-detector time
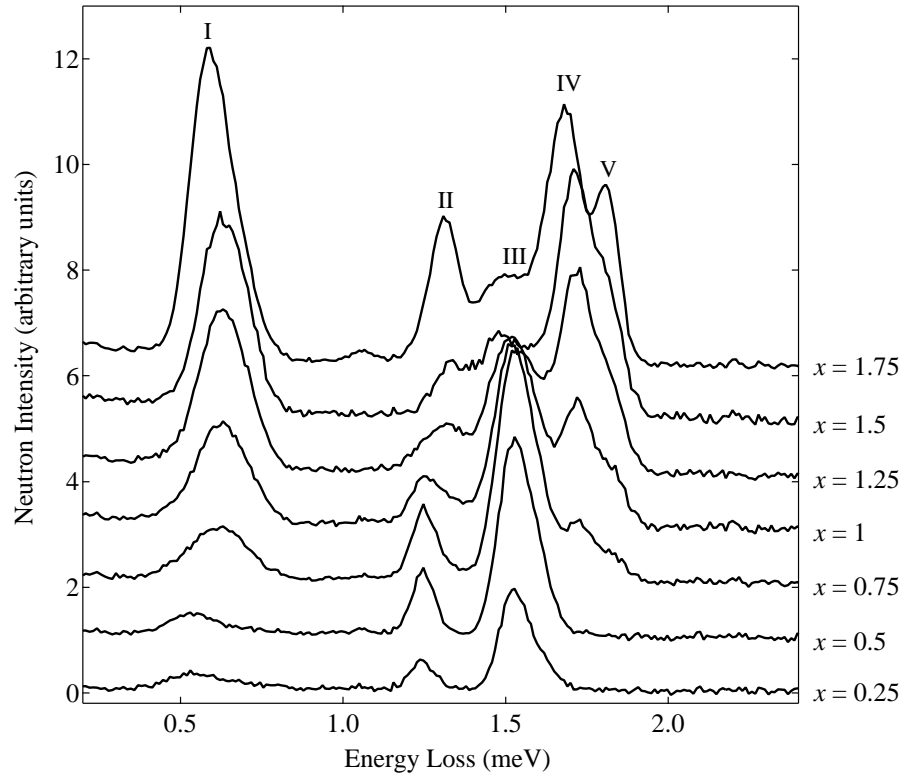
Figure 6.3: Low-energy IINS spectra of $KC_{24}(H_2)_x$ as a function of increasing H_2 concentration. Scattering from bare KC_{24} has been subtracted. Spectra are vertically offset for clarity.

of 1500. These settings give a resolution of about $120\,\mu eV$ at the elastic line and a resolution

of about $90\,\mu eV$ at an energy transfer of $1\,meV$. The maximum energy loss that can be mea-

sured is roughly $2.79\,meV$. The momentum-transfer range is about $0.1\,\text{Å}^{-1}$ to $2.5\,\text{Å}^{-1}$ at

the elastic line, and roughly $0.7\,\text{Å}^{-1}$ to $1.8\,\text{Å}^{-1}$ at the maximum energy transfer. The IINS

spectra were reduced from the $S(Q,\omega)$ by summing over the complete momentum-transfer

range and grouping the counts into energy bins of $0.01\,meV$ width. For diffraction patterns,

the $S(Q,\omega)$ was summed over the nearly-elastic interval $-0.1\,meV$ to $0.1\,meV$ and binned

into $0.008\,\text{Å}^{-1}$ increments. Once again, scattering from H_2 was isolated by subtracting the

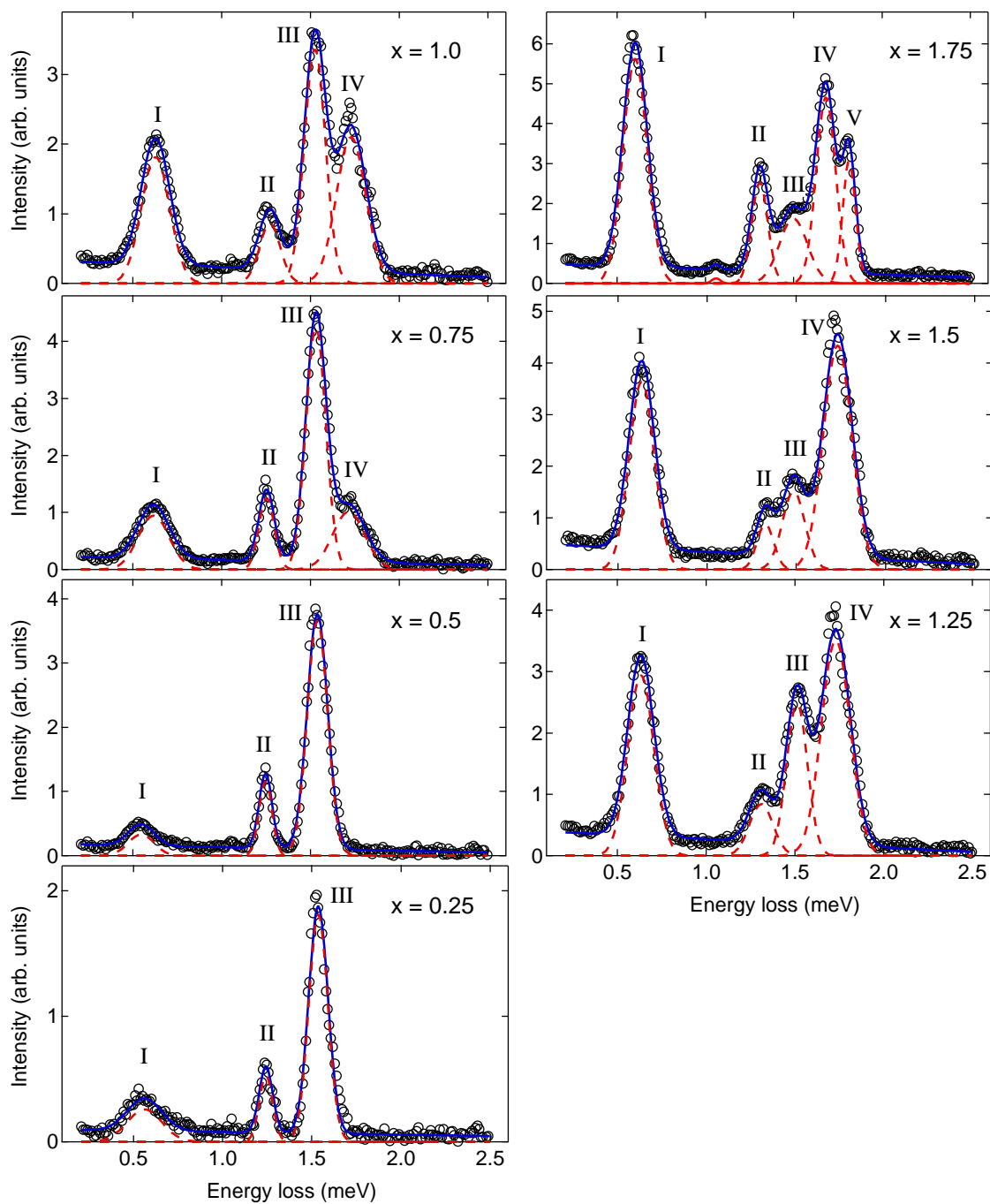scattering from bare KC_{24}. Normal H_2 was used for all measurements on DCS.

Figure 6.4: Decomposition of the low-energy-transfer IINS spectra of $KC_{24}(H_2)_x$ into a sum of Gaussian curves (plus a flat background which is not pictured).

Table 6.1: Summary of peak positions and peak areas of the low-energy IINS spectra

	Peak I		Peak II		Peak III		Peak IV		Peak V	
x^a	Center (meV)	Area (a.u.)	Center (meV)	Area (a.u.)	Center (meV)	Area (a.u.)	Center (meV)	Area (a.u.)	Center (meV)	Area (a.u.)
0.25	0.56	0.06	1.24	0.05	1.54	0.24				
0.50	0.55	0.06	1.25	0.11	1.54	0.53				
0.75	0.62	0.21	1.25	0.14	1.53	0.59	1.72	0.23		
1.00	0.63	0.36	1.27	0.13	1.53	0.50	1.73	0.43		
1.25	0.63	0.54	1.31	0.14	1.51	0.37	1.73	0.72		
1.50	0.63	0.64	1.33	0.10	1.49	0.24	1.73	0.87		
1.75	0.60	0.96	1.31	0.29	1.50	0.32	1.68	0.64	1.81	0.28

[a] Denotes the H_2 composition of a $KC_{24}(H_2)_x$ sample
[b] Errors not listed for the fit parameters

6.4   Results

6.4.1   Low-energy IINS spectra

Low-energy-transfer IINS spectra of $KC_{24}(H_2)_x$ collected on DCS are shown in Fig. 6.3. Background scattering from bare KC_{24} has been subtracted. The spectra contain at least five distinct peaks whose intensities vary with H_2 concentration. To determine peak locations and areas, the spectra were decomposed into a sum of Gaussian curves plus a flat background. The results of these fits are shown in Fig. 6.4. Even at the lowest hydrogen concentration, there are three distinct peaks. Peaks I and II appear to shift gradually to higher energy as the hydrogen concentration is increased. Due to the finite instrument resolution, though, it is not really possible to distinguish the fine structures of peaks containing features narrower than 90 μeV. Interestingly, there is a fairly strong transfer of intensity from peak III to peak IV as the H_2 loading is increased. At the highest hydrogen loadings, peak IV appears to split into peak IV and peak V. The presence of distinct low-energy peaks in the IINS spectrum are likely an indicator of distinct adsorption sites for H_2 in KC_{24} as described in greater detail in the discussion section. Changes in the fine structure of peaks may be caused by increasing interactions between the H_2 molecules as the concen-
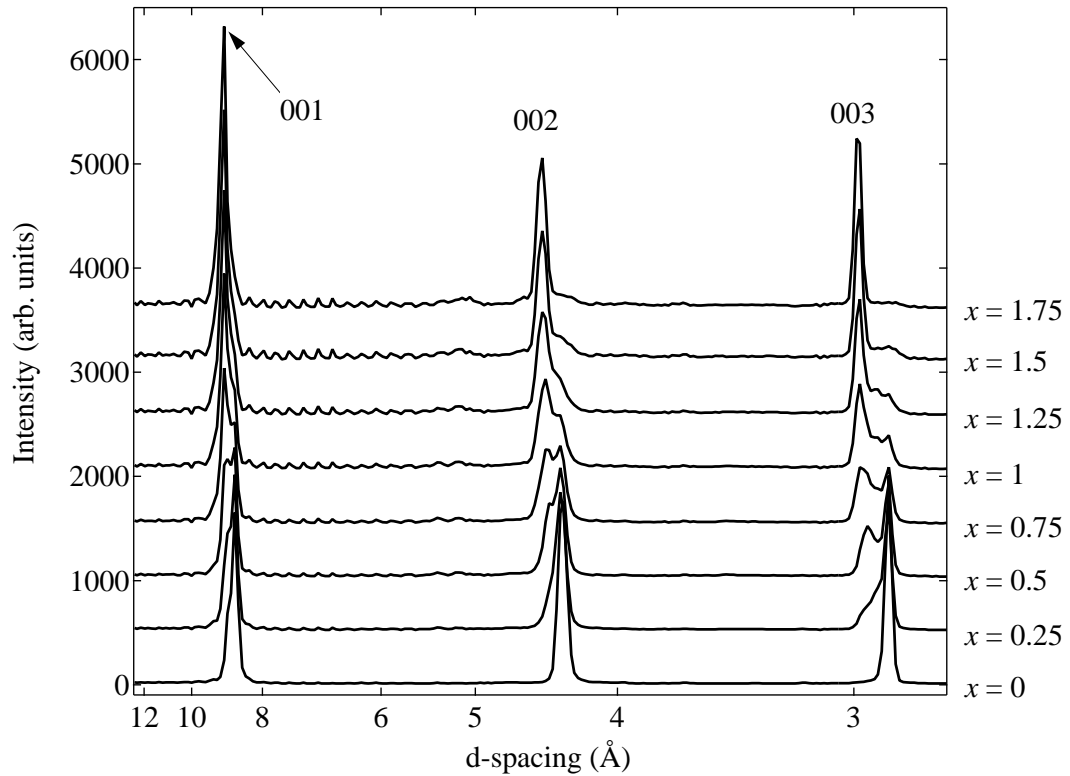
Figure 6.5: Diffraction pattern of $KC_{24}(H_2)_x$ measured on DCS at $4\,K$.

tration increases. However, the collapse of peak III, and associated growth of peak IV, may

indicate a reconstruction of the in-plane KC_{24} lattice. Similar behavior has been noted for

the $CsC_{24}(H_2)_x$ system [112]. Peak positions and areas for the low-energy IINS spectra are

summarized in Table 6.1.

6.4.2 Diffraction pattern from low-energy IINS spectra

The DCS instrument contains an angular array of detectors from which diffraction informa-

tion can be obtained by the time-of-flight method. It should be emphasized that DCS is *not*

optimized as a diffractometer, and that the resolution in Q is quite coarse. Nevertheless,

a qualitative diffraction pattern can be extracted from the measured $S(Q, \omega)$ by plotting

the integrated intensity under the elastic peak as a function of momentum-transfer. The

diffraction pattern obtained from the low-energy IINS measured on DCS is illustrated in Fig. 6.5. For the $x = 0$ filling, the (001), (002), and (003) reflections have a d-spacing of 8.73 Å, 4.33 Å, and 2.90 Å, respectively. This translates to an average KC_{24} interlayer spacing of 5.34 Å. As H_2 is introduced to the sample, there is a gradual transfer of intensity to the second set of peaks with a slightly larger d-spacing. The fully hydrogenated sample has an interlayer spacing of 5.63 Å. In other words, the adsorption of H_2 causes the KC_{24} layers to expand by about 5%. These results are fully consistent with data reported in Ref. [64]. Given the low Q-resolution of the instrument, a quantitative analysis of diffraction data is not appropriate. Nevertheless, the diffraction data verifies three things. First, the KC_{24} sample is not contaminated by stage-1 or stage-3 compounds. Second, hydrogen is being adsorbed between the layers of KC_{24} resulting in an expansion of the interlayer spacing. Finally, the fact that there is a transfer of intensity between two distinct, co-existent peaks, rather than the shift of a single peak, implies that $KC_{24}(H_2)_x$ contains co-existent regions of the hydrogenated and pure KC_{24} phase.

6.4.3 Intermediate and high-energy IINS spectra

Intermediate-energy IINS spectra of $KC_{24}(pH_2)_x$ were measured as a function of hydrogen filling on the FANS instrument using the PG(002) monochromator. They are displayed in Fig. 6.6. As explained in the methods section, *para*-hydrogen was used instead of normal hydrogen to simplify the interpretation of spectral peaks. To determine peak positions and areas, the intermediate-energy spectra were fitted to a sum of Gaussian curves plus a flat background, and the fits are indicated in the figure. At the two lowest hydrogen fillings of $x = 0.2$ and $x = 0.5$, the spectra appear similar, except for the overall increase in intensity with hydrogen concentration. Peak I (11.9 meV) and Peak II (29.2 eV) are the dominant
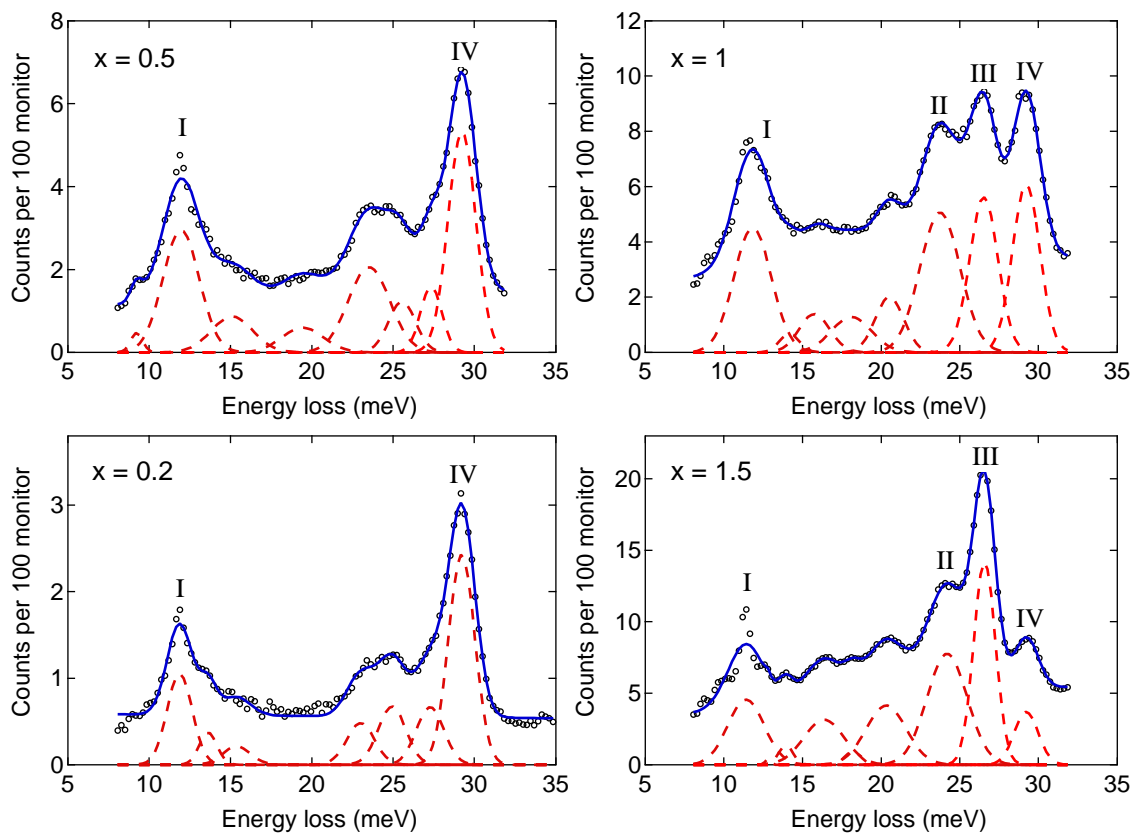
Figure 6.6: Intermediate-energy IINS spectra of $KC_{24}(pH_2)_x$ as a function of hydrogen filling. Solid blue lines represent fits to a sum of Gaussian curves plus a flat background. Individual Gaussian curves are plotted as dashed red lines. Flat background is not shown. Data points below $8\,meV$ and above $32\,meV$ were removed prior to the nonlinear regression fit.

features. Nascent peaks at $23\,\mathrm{meV}$ and $25\,\mathrm{meV}$ are somewhat difficult to distinguish from the large background intensity. As hydrogen filling is increased to $x = 1$, two new peaks emerge at $23.7\,\mathrm{meV}$ (Peak II) and $26.5\,\mathrm{meV}$ (Peak III). As hydrogen composition is further increased to $x = 1.5$, there is a strong increase in Peak III, but little increase in the other peaks. The sharp feature that appears at Peak I at the $x = 1.5$ filling may be an instrument artifact from $\lambda/2$ contamination of the incident beam, due to the large transition ca. $50\,\mathrm{meV}$. In all of the intermediate-energy spectra, there is a large background intensity which may be due to the overlap of closely-spaced peaks. With the modest energy resolution of FANS (i.e., $1.2\,\mathrm{meV}$), however, individual peaks are often difficult to distinguish. Peak positions and areas for the intermediate-energy IINS are summarized in Table 6.2.

High-energy IINS spectra of $\mathrm{KC}_{24}(p\mathrm{H}_2)_x$ are plotted in Fig 6.7 as a function of hydrogen filling. Spectra were only measured for $x = 0.5$ and $x = 1.0$. The dominant feature in both spectra is Peak VII, which has a greater intensity than any other peak. It should be noted that the curves in Fig 6.7 are not artificially offset. The vertical offset is due to the large background intensity, which may indicate a large amount of H_2 recoil associated with the scattering. At the higher $x = 1.0$ filling, upon closer examination, Peak VII appears to have a fine structure comprising two sub-peaks. The increase in intensity of the lower-energy sub-peak is what causes the apparent shift of the total peak from $50.9\,\mathrm{meV}$ at $x = 0.5$ to $49.4\,\mathrm{meV}$ at $x = 1$. Peak positions and areas for the high-energy IINS spectra are listed in Table 6.2.

6.4.4   IINS spectra of HD and D_2 adsorbed in KC_{24}

The richly-structured IINS spectra of $\mathrm{KC}_{24}(p\mathrm{H}_2)_x$ contain numerous overlapping peaks, making it difficult to accurately identify and interpret the origins of the spectral features. One method of obtaining more information from the inelastic spectra is to substitute the
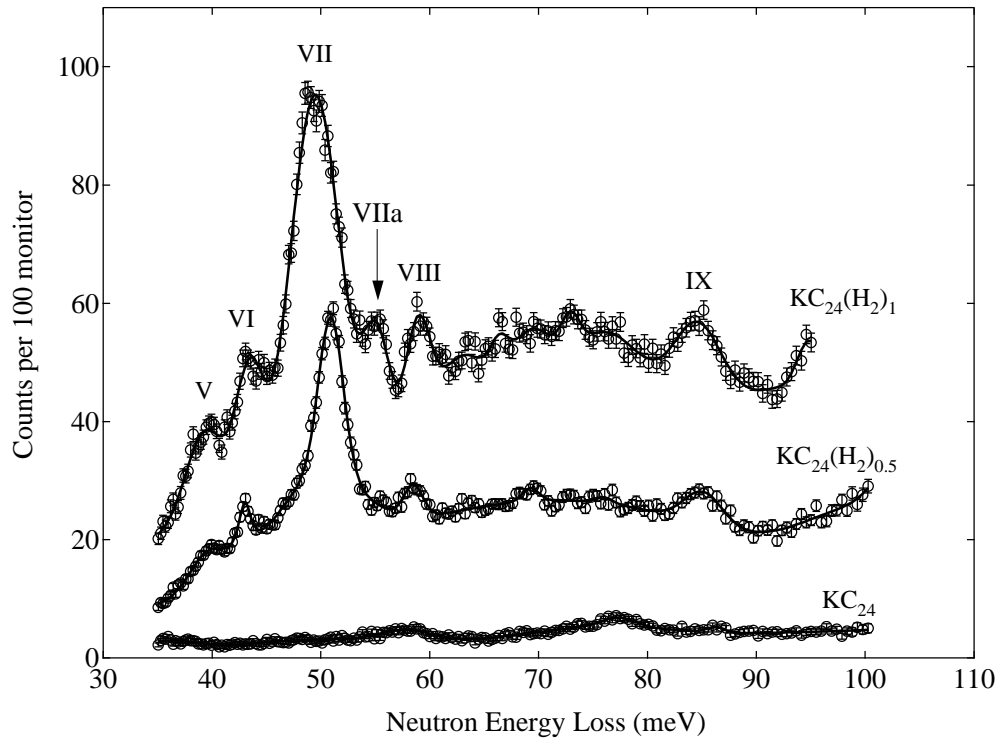
Figure 6.7: High-energy IINS spectra of $KC_{24}(pH_2)_x$ measured with the Cu(022) monochromator. Solid lines represent fits to a sum of Gaussian curves plus flat background. Individual curves are *not* manually offset.

Table 6.2: Summary of peak positions and peak areas of the intermediate and high-energy IINS spectra

	$x = 0.2$		$x = 0.5$		$x = 1.0$		$x = 1.5$	
Peak	Center (meV)	Area (a.u.)	Center (meV)	Area (a.u.)	Center (meV)	Area (a.u.)	Center (meV)	Area (a.u.)
I	11.9	2.02	11.8	5.84	11.8	13.4	11.4	13.2
II					23.7	16.2	24.2	24.8
III					26.5	12.7	26.6	24.6
IV	29.2	4.94	29.3	8.71	29.2	13.3	29.2	7.10
V			39.4	2.83	39.4	71.6		
VI			43.0	21.1	43.5	71.3		
VII			50.9	93.8	49.4	360.		
VIII			58.5	7.76	59.1	33.2		
IX			85.2	27.2	84.7	37.9		

[a] Peak parameters were obtained from fitting the spectra to a sum of Gaussian curves plus a flat background.

[b] Peaks I–IV are from the PG(002) spectra (see Fig. 6.6), while peaks V–IX are from the Cu(220) spectra (see Fig. 6.7). The integrated areas from the two different spectra are not directly comparable.

H_2 adsorbate with a hydrogen isotope containing a different mass, specifically HD and D_2. Shifts in peak positions as a function of mass can sometimes reveal the rotational or vibrational origin of a spectral peak. For a pure rotational transition of a free diatomic molecule, energy is proportional to the inverse of the reduced mass (see Eq. 6.2). Relative to H_2, the rotational transitions of HD will be reduced by a factor of 0.75, and for D_2 they will be reduced by a factor of 0.5. For a whole-molecule vibrational mode (i.e., governed by a power-law potential $V(x) = Ax^2$), the energy levels scale with mass as $m^{-1/2}$. Relative to H_2, the vibrational transitions of HD will be reduced by a factor of $\sqrt{2/3} \approx 0.82$, and for D_2 the transitions will be reduced by a factor of $\sqrt{1/2} \approx 0.71$.

IINS spectra were collected for HD and D_2 samples.[1] These spectra are compared with the p-H_2 spectra in the three panels of Fig. 6.8. Ratios between the peak positions for the three isotopes are summarized in Table 6.3. Unfortunately, it is difficult to identify the peaks for each isotope which correspond to the same transition. This is especially true for HD, which contains a complex spectrum due to the absence of symmetry restrictions on the rotational and nuclear spin states. Figure 6.8 contains my best guess for the peaks which correspond to equivalent transitions. Peaks are labeled with either an "a", "b" or "c" depending on whether the isotope is H_2, HD, or D_2, respectively.

The only peak ratio which can be easily categorized is Peak I, which seems to follow the $m^{-1/2}$ scaling expected for a pure vibrational transition. However, the cross-section of p-H_2 for a pure vibrational transition (with no change in the rotational level) is proportional to σ_c and is very small (see Sec. 6.2.4). Peaks originating from pure phonon excitations should not be visible in the spectrum of $KC_{24}(pH_2)_{0.5}$. Since the cross-section for a one-phonon

---

[1] Due to the smaller scattering cross-section of deuterium, it was necessary to collect data for a considerably longer time period. Even with longer collection times, the error bars on the D_2 spectra are much larger than those of the other samples.
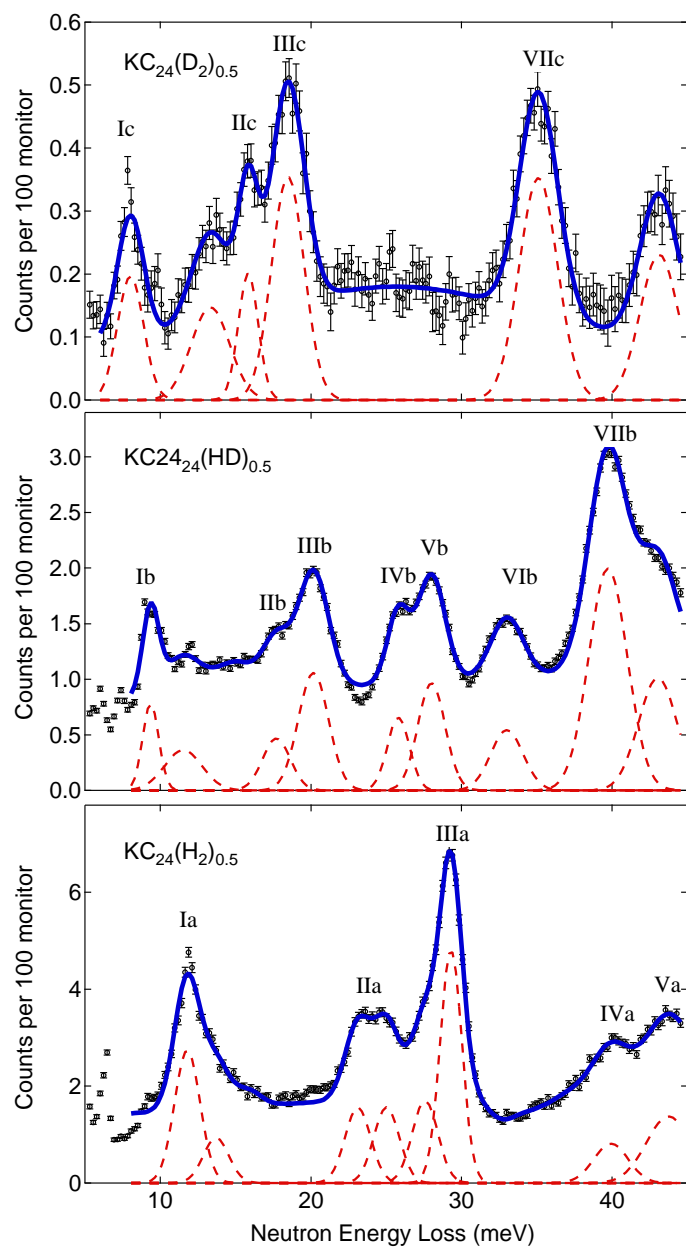
Figure 6.8: Intermediate-energy IINS spectra of D_2, HD, and p-H_2 adsorbed in KC_{24}. Solid lines represent fits to a sum of Gaussian curves plus a flat background. The Gaussian curves are shown as dashed, red lines. Fit components not corresponding to a clear, discrete peak are not illustrated. Peaks thought to correspond to the same transition are labeled with the same Roman numeral, with an "a", "b" or "c" to identify the isotope.

Table 6.3: Peaks positions in the intermediate IINS spectra for different hydrogen isotopes

Peak	H_2 Position[a]	HD Position	HD/H_2 Ratio	D_2 Position	D_2/H_2 Ratio
I	11.9	9.36	0.79	8.02	0.68
II	24.1	18.1	0.75	15.9	0.66
III	29.3	20.2	0.69	18.5	0.63
IV	39.9	25.8	0.65		
V	43.8	28.0	0.64		
VI		33.0			
VII		43.0		35.1	

[a] H_2 peak positions were obtained from the p-H_2 spectra.
[b] Peak positions are reported in units of meV.
[c] Composition was $x = 0.5$ for all isotopes.
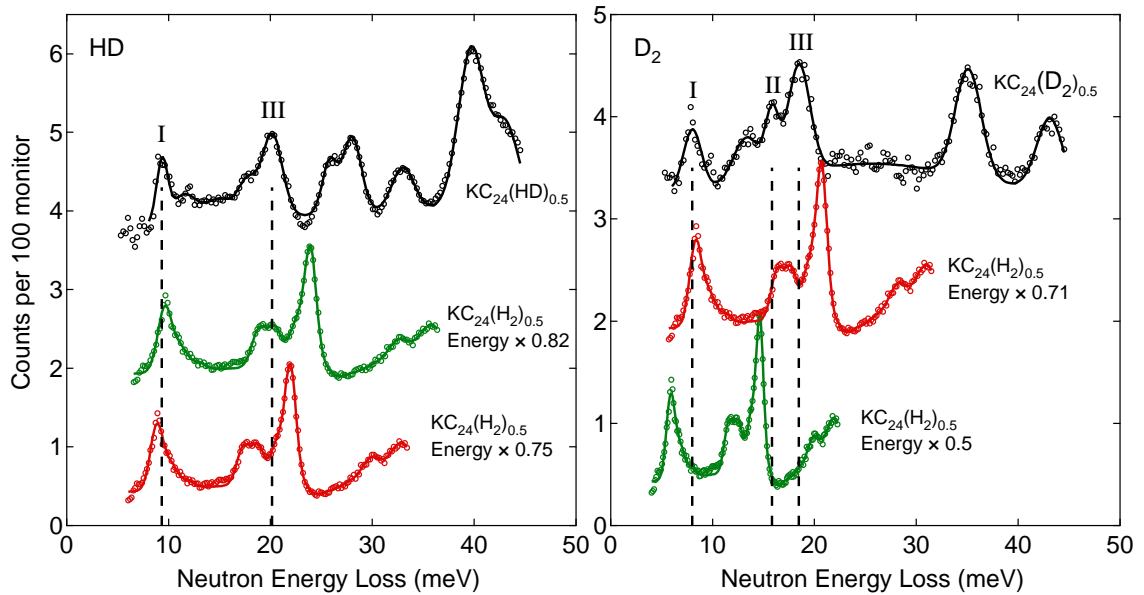
Figure 6.9: Comparison of the IINS spectra of the p-H_2, HD, and D_2 loaded samples. The p-H_2 spectra have been rescaled along the energy axis with the μ^{-1} factor ($\times 0.75$ for HD and $\times 0.5$ for D_2) of a pure rotational transition and the $m^{-1/2}$ factor ($\times 0.82$ for HD and $\times 0.71$ for D_2) of a pure phonon transition.

+ one-rotational multi-excitation in p-H_2 contains the large incoherent scattering length, many of the spectra features may therefore be due to multi-excitation transitions.

Isotopic shifts in the IINS spectra are directly compared in Fig. 6.9. The p-H_2 spectra are rescaled on the energy axis with the μ^{-1} factor of a pure rotational transition and the $m^{-1/2}$ factor of a pure phonon transition. In this manner, peak positions for the isotopes can be directly compared to determine whether there are any good matches. Once again it is evident that none of the peaks (except for Peak I) follow the simple scaling relations expected for a pure phonon or rotational transition.

6.5 Hydrogen bound states studied by DFT

6.5.1 Computational details

To estimate the energy levels of H_2 bound states in KC_{24}, first-principles calculations were performed using density function theory (DFT), as implemented in the Vienna *Ab intio* Simulation Package [113]. A plane-wave basis set was used with a projector-augmented-wave potential and a Perdew-Burke-Ernzerhof exchange-correlation functional in the generalized gradient approximation (GGA) [114]. Although GGA does not treat the correlations between electron fluctuations which give rise to van der Waals interactions, it can still be used to calculate the electrostatic and orbital interactions. In general, GGA is known to underbind H_2 in physisorption systems with significant van der Waals contributions.

The theoretical $\left(\sqrt{7} \times \sqrt{7}\right) R\,19.11°$ structure with chemical formula KC_{28} was used for the in-plane potassium structure. A stacking sequence for the potassium layers was generated by translating each layer 1.41 Å (i.e., equal to the C$-$C bond length) in the direction of the x-axis.[2] This sequence of potassium layers repeats after 21 layers. The graphite stacking

[2]See the top panel of Fig. 6.13 for the orientation of the x and y axes.

sequence follows the standard A|AB|BC|CA pattern (see Fig. 2.2a). Three-dimensional periodic boundaries are applied to the unit cell. The c-axis interlayer spacing of the $KC_{28}(H_2)_1$ compound was optimized at $5.4\,\text{Å}$, but all other geometrical parameters were fixed at their theoretical values. To sample the Brillouin zone, a Gamma-centered k-point grid was generated. Based on convergence tests, it was found that a plane-wave basis set energy cutoff of $500\,\text{eV}$ and a $8 \times 8 \times 6$ k-point grid was necessary to obtain an accuracy of $1\,\text{meV atom}^{-1}$. Due to limited computational resources, however, a plane-wave cutoff of $300\,\text{meV}$ was used in conjunction with a $4 \times 4 \times 3$ k-point grid. Lattice parameters and atom positions were held fixed at their theoretical values for the $\left(\sqrt{7} \times \sqrt{7}\right) R\,19.11°$ structure. These calculations must therefore be considered as qualitative rather than quantitative. The potential energy surface can still provide useful insights into bound states of the H_2 molecule.

6.5.2   Results

Total ground state energies were calculated as a function of H_2 center-of-mass position and molecular orientation. First, the potential energy surface of the $KC_{28}(H_2)_1$ system was sampled over a grid of 58 positions within the unit cell, with the H_2 molecule oriented perpendicular to the basal plane, and vertically centered in the gallery. The results are illustrated in Fig. 6.10. The contribution of both the graphite corrugation potential and the $K–H_2$ interaction are evident from the results. Because the H_2 molecule was oriented vertically, the repulsive interactions between the hydrogens and the carbons are substantial. The local minima are located near the hexagon centers.

The general goal of these first-principles calculations is to determine the energy levels of bound center-of-mass H_2 vibrational modes (i.e., phonons). Thus, a complete calculation would involve the construction and diagonalization of the classical, three-dimensional
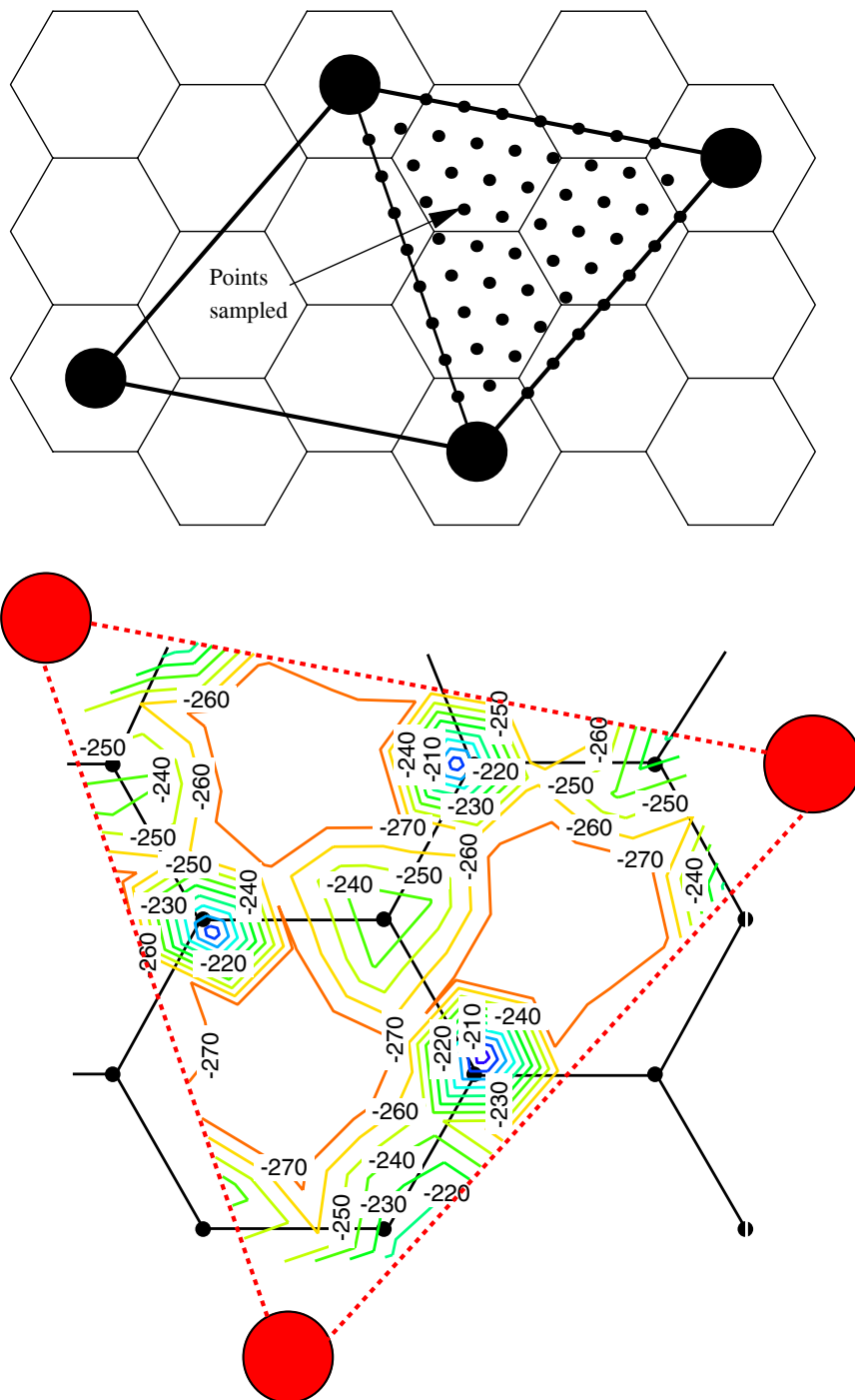
Figure 6.10: Top: Grid of 58 H_2 center-of-mass positions within the KC_{28} unit cell for which the total ground state energy was calculated. Bottom: Potential energy surface constructed from the grid of calculated ground state total energies. The H_2 molecule was oriented perpendicular to the graphite basal plane.

force-constant matrix for the H_2 center-of-mass at the minimum in the PE surface. This calculation is quite computationally expensive for the large $KC_{28}(H_1)_1$ unit cell. An approximation of the phonon energy levels can be calculated from 1D slices through the center-of-mass PE surface.

As shown in Fig. 6.11, one-dimensional slices through the PE surface were calculated along the in-plane paths labeled "scan-1" and "scan-2." Energies were also calculated along the z-axis (out-of-plane) through the point labeled E_{min} in Fig. 6.11, but are not illustrated. The H_2 molecule was oriented perpendicular to the basal plane for all calculations. The energy minimum for all three scans occurs at point E_{min}, which has a K–H_2 distance of about $2.7\,\text{Å}$. Neglecting all other degrees of freedom, the 1D Schrödinger equations were solved for the three calculated potential energy wells using the Fourier grid Hamiltonian method [115]. The quantum energy levels are displayed in Fig. 6.11 as dashed lines. For scan 1, the fundamental $n(0 \rightarrow 1)$ transition occurs at $8\,\text{meV}$, with an overtone at $26\,\text{meV}$. For scan-2, the fundamental transition is at $12\,\text{meV}$, with an overtone at $25\,\text{meV}$. For out-of-plane translations, the fundamental transition occurs at $77\,\text{meV}$, well above the spectral peaks under consideration.

The total energy of the H_2 molecule was calculated along scan-1 for three different orientations. Results are shown in Fig. 6.12. The 'tee" and "aligned" orientations are both in-plane, while the "vertical" orientation is out-of-plane. Based on these results, it can be seen that the energy minimum is strongly coupled to the molecular orientation. Having the H_2 molecule aligned towards the potassium increases a repulsive interaction at short separations. This implies that there is a significant amount of rotational-translational coupling in the KC_{24}-H_2 system.

The rotational potential was calculated over an 18×24 grid of H_2 orientations (θ, ϕ).
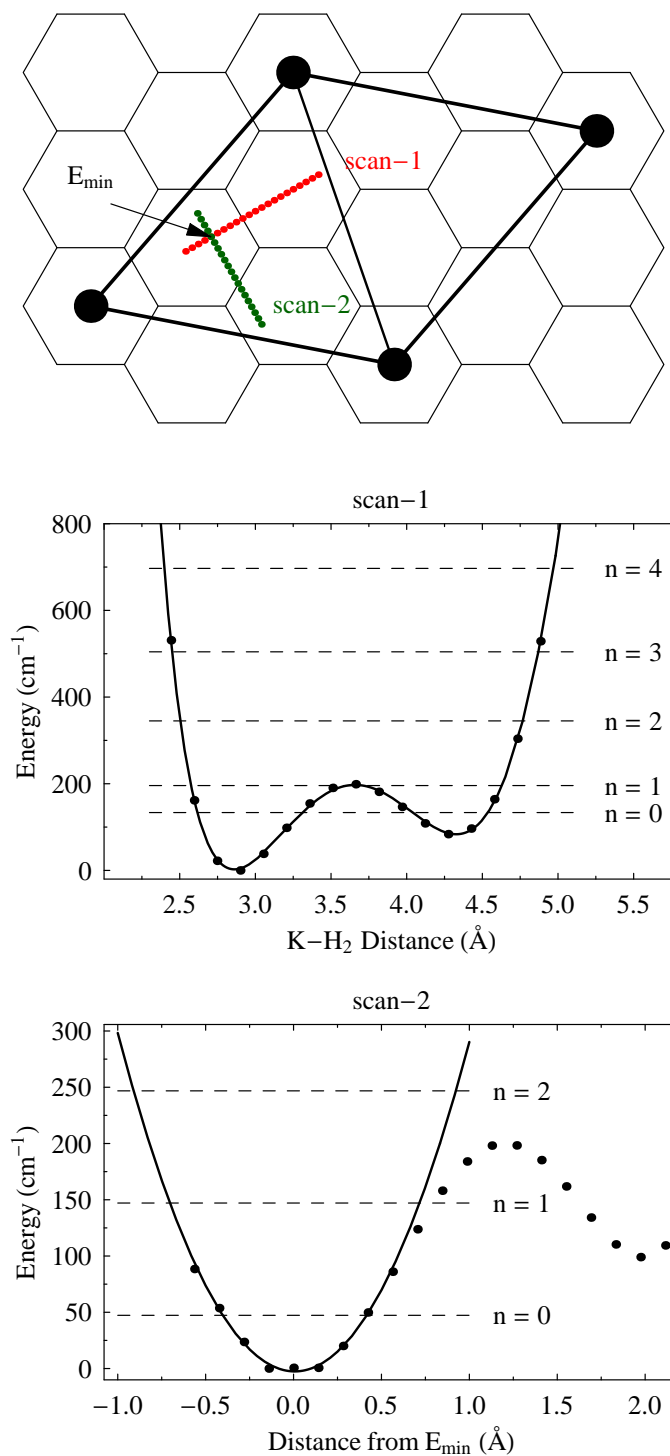
Figure 6.11: Top: One-dimensional slices through the potential energy surface. The H_2 molecule was oriented perpendicular to the basal plane for both scans. Middle: Potential energy well for scan-1. Bottom: Potential energy well for scan-2. Quantum energy levels are plotted as dashed lines. Note that energies are reported in units of cm^{-1}.
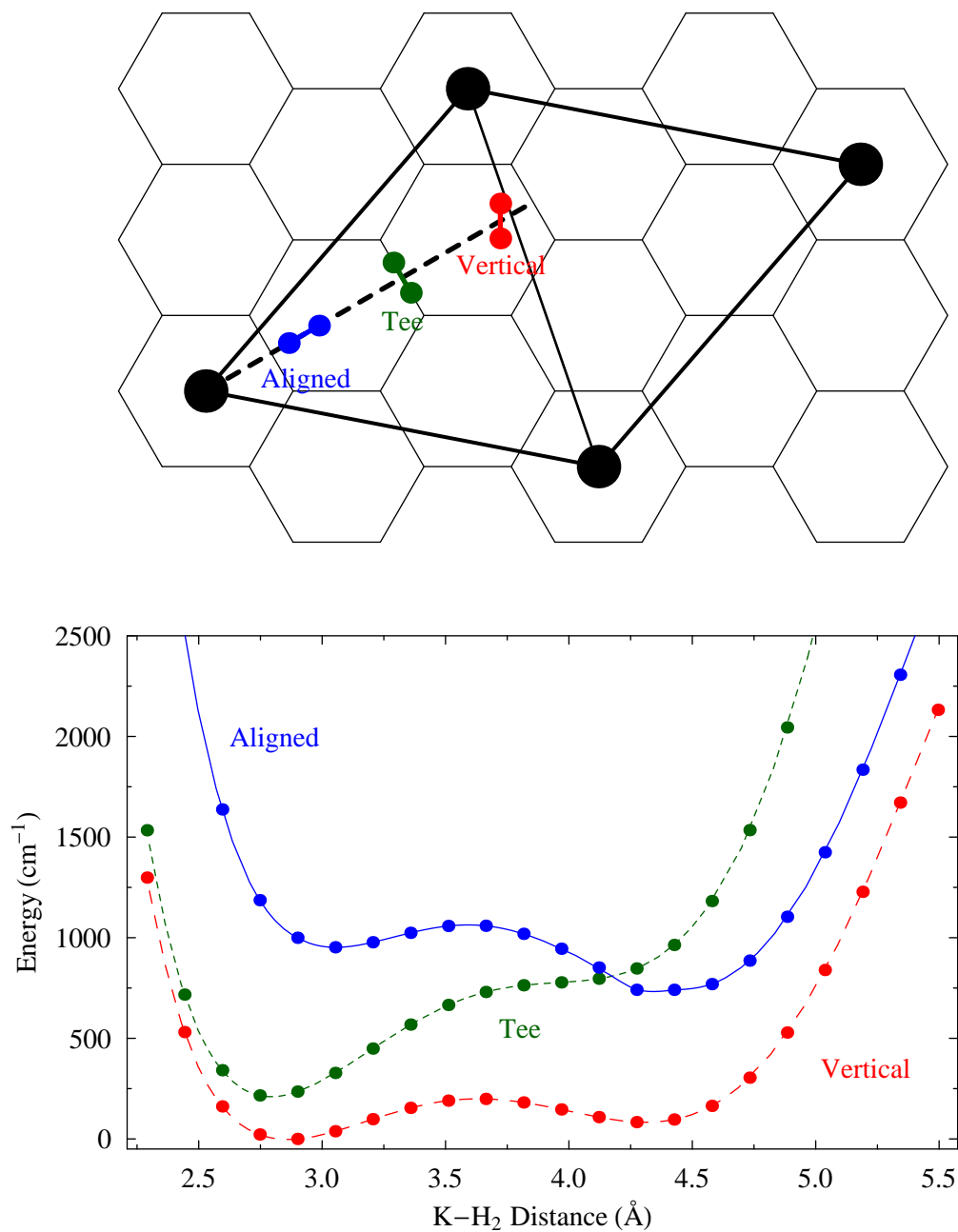
Figure 6.12: Top: Three different orientations of the H_2 molecule as it is moved along the $K-H_2$ axis indicated by the dashed line. The *tee* and *aligned* orientations are both parallel to the basal plane (in-plane), while the *vertical* orientation is perpendicular to the basal plane (out-of-plane). Bottom: Total energy of the H_2 molecule as a function of $K-H_2$ distance for the three orientations of the molecule. Note that energy is reported in units of cm^{-1}.
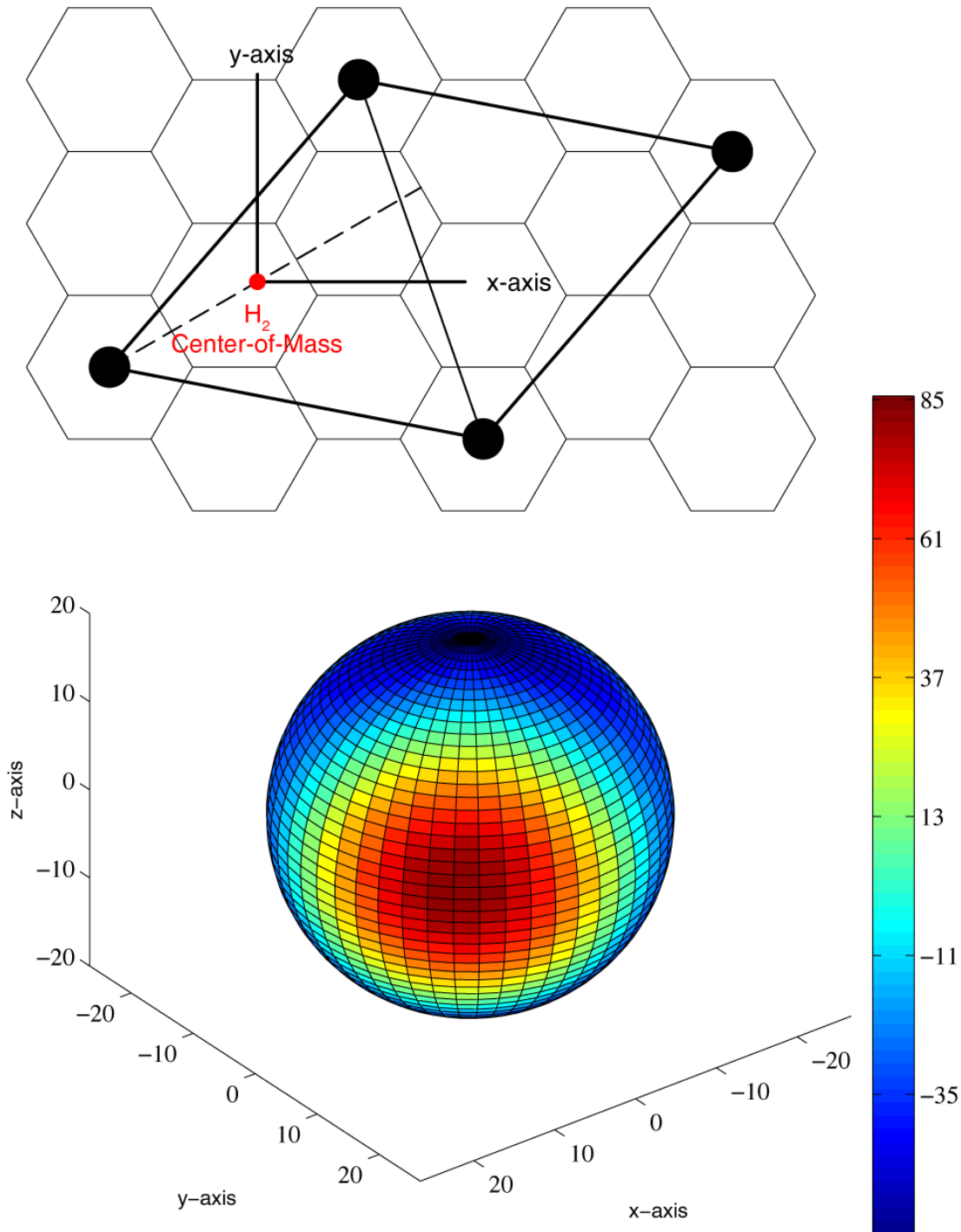
Figure 6.13: Top: Coordinate system which describes the H_2-orientation. The x and y axes are both in-plane, while the z axis is out-of-plane. The H_2 center-of-mass is fixed at the energy minimum. Bottom: Contour plot of the rotational potential mapped onto a sphere representing the H_2 orientation (ϕ, θ). This coordinate system is consistent with the one depicted in the top panel.

We define θ as the angle between the H_2 molecular axis and the z-axis, and ϕ as the angle between the x-axis and the projection of the H_2 molecular axis along the x-y-plane. For all calculations the H_2 center-of-mass was fixed at the minimum energy site roughly $2.7\,\text{Å}$ from the potassium center and centered between the graphite planes. The calculated orientational potential is illustrated in the bottom panel of Fig. 6.13. The red color corresponds to the energy maximum while the blue color indicates the energy minimum. It is clear that the maximum energy occurs when the H_2 molecule is pointed directly at the potassium in an "aligned" formation. The minimum energy orientation occurs for either a "tee" or "vertical" formation, with the H_2 molecule facing the potassium side-on. The rotational potential is very well-described by a two-dimensional, anisotropic hindered rotor potential,

$$V(\theta, \phi) = \frac{a + b\sin(2\phi + c)}{2}(1 - \cos 2\theta), \tag{6.11}$$

where $a = 72.92\,\text{meV}$, $b = -47.65\,\text{meV}$ and $c = -158.6°$. The extra phase factor, c, does not affect the rotational energy levels of the system and is ignored in the remaining calculations. Hamiltonian matrix elements were calculated for a spherical harmonics basis set, $\{Y_0^0, Y_1^{-1}, Y_1^0, Y_1^1, \ldots, Y_6^6\}$. The resulting 49×49 matrix has the form,[3]

$$\hat{H} = \begin{pmatrix} E_0 + \langle Y_0^0|V|Y_0^0\rangle & \langle Y_0^0|V|Y_1^{-1}\rangle & \cdots & \langle Y_0^0|V|Y_6^6\rangle \\ \langle Y_1^{-1}|V|Y_0^0\rangle & E_1 + \langle Y_1^{-1}|V|Y_1^{-1}\rangle & \cdots & \langle Y_1^{-1}|V|Y_6^6\rangle \\ \vdots & \vdots & \ddots & \vdots \\ \langle Y_6^6|V|Y_0^0\rangle & \langle Y_6^6|V|Y_1^{-1}\rangle & \cdots & E_6 + \langle Y_6^6|V|Y_6^6\rangle \end{pmatrix} \tag{6.12}$$

---

[3]For slightly better numerical accuracy, a 64×64 matrix is recommended [116]. Due to the somewhat qualitative nature of the rotational potential, the current matrix size is probably sufficient for estimating the rotational energy levels.
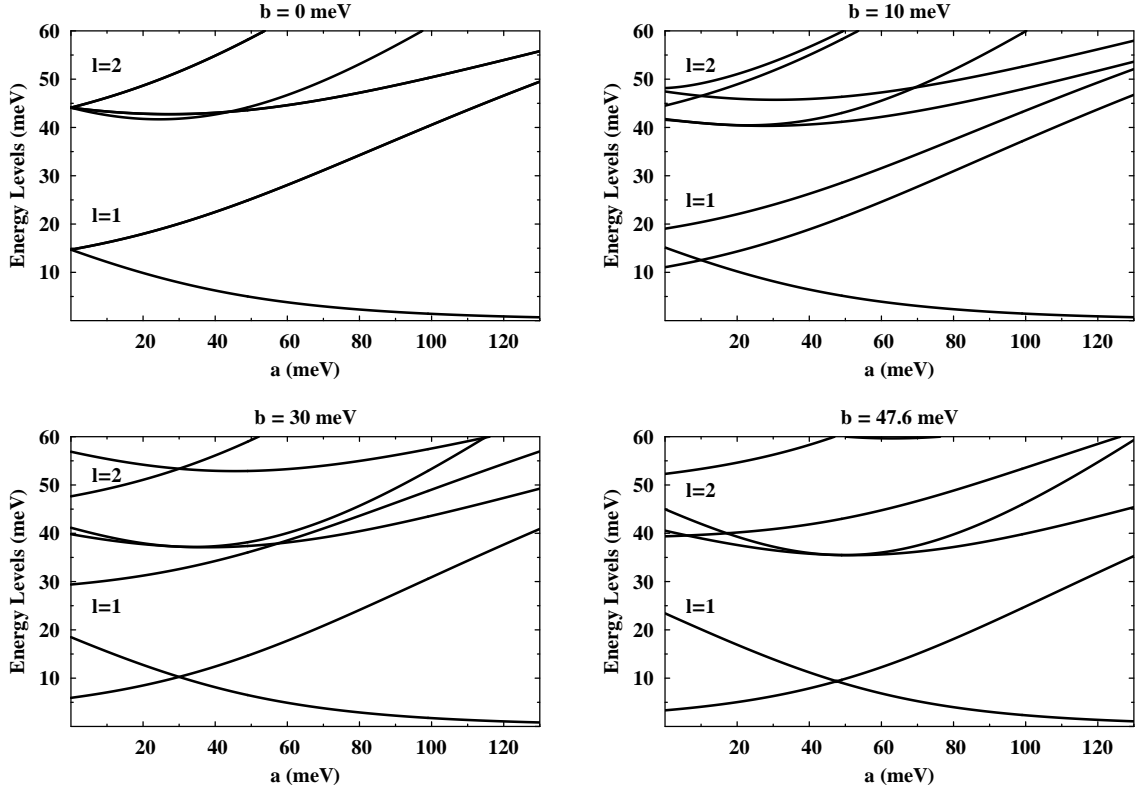
Figure 6.14: Energy levels for a two-dimensional, anisotropic hindered rotor model relative to the ground $l = 0$ state. Energies are plotted as a function of the θ-based rotational barrier, a, and evalulated for four different values of the ϕ-based azimuthal rotational barrier, b.

where $E_l = l(l+1)B_{\text{rot}}$, and the inner products are equal to

$$\langle Y_{l'}^{m'}|V|Y_l^m\rangle = \int_0^{2\pi}\int_0^{\pi} Y_{l'}^{m'}(\theta,\phi)^*V(\theta,\phi)Y_l^m(\theta,\phi)\sin\theta d\theta d\phi. \tag{6.13}$$

Eigenenergies were determined from an exact diagonalization of the matrix. In Fig. 6.14 the calculated rotational energy levels for the $l = 1$ and $l = 2$ states, relative to the $l = 0$ state, are plotted as a function of a for two different values of b. For $b = 0$ we recover the familiar one-dimensional hindered rotor model, in which the $l, m(1, \pm 1)$ energy levels are degenerate. For non-zero values of b this degeneracy is lifted. Transition energies for the calculated orientational potential ($a = 72.92\,\text{meV}$, $b = -47.65\,\text{meV}$) occur at $4.9\,\text{meV}$,

15.9 meV, 36.4 meV, 38.0 meV and 47.3 meV, consistent with the values reported in Ref. [64]. Unfortunately, these values are clearly inconsistent with the experimental peak positions. Therefore, introducing a large ϕ-dependence into the orientation potential does not appear to be realistic. As described in the next section, a simple one-dimensional hindered rotor model, evaluated at three different barrier heights, does a much better job of describing the spectral peaks at both low energies and high energies. One possible explanation is that quantum delocalization of the H_2 center-of-mass over the three minimum-energy sites (see Fig. 6.10) results in an effective potential that does not have a ϕ-dependence [64].

6.6   Discussion

The IINS data of $KC_{24}(H_2)_x$ contains a complex progression of spectral peaks. Based on previous studies of RbC_{24} and CsC_{24} [51, 64, 65, 117, 118], it is known that the low energy peaks (ca. 1 meV) and the high energy peaks (ca. 50 meV) originate from the splitting of the $l(0 \rightarrow 1)$ rotational transition in the presence of a strong anisotropic field. The one-dimensional hindered rotor model provides a reasonable description of the peak positions, but requires the presence of multiple barrier heights. Referring to Fig. 6.1, it can be verified that a rotational barrier height of 139 meV corresponds to peak positions at 0.56 meV and 52 meV, which does match experimental peak positions in the $KC_{24}(H_2)_{0.5}$ spectrum. Barrier heights of 105 meV and 96 meV provide good matches to other peaks in the $KC_{24}(H_2)_{0.5}$ and $KC_{24}(H_2)_1$ spectra, as summarized in Table 6.4. These values also compare well with rotational barrier heights determined from first-principles calculations, which varied up to 121 meV for an H_2 molecule fixed at the energy minimum in the center-of-mass PE surface.

The need for multiple rotational barrier heights is consistent with the existence of dif-

Table 6.4: Transition energies predicted by the one-dimensional hindered rotor model compared to experimental peak positions for the $KC_{24}(H_2)_{0.5}$ and $KC_{24}(H_2)_1$ samples

(a) 1D-type Potential ($V_2 > 0$)

$KC_{24}(H_2)_{0.5}$			$KC_{24}(H_2)_1$		
Barrier Height (meV)	$\Delta E_1{}^a$ (meV)	$\Delta E_2{}^b$ (meV)	Barrier Height (meV)	ΔE_1 (meV)	ΔE_2 (meV)
139	0.56 $(0.55)^c$	52.0 (50.9)	133	0.63 (0.63)	50.3 (49.4)
105	1.25 (1.25)	42.1 (43.0)	105	1.24 (1.27)	42.1 (43.5)
96	1.55 (1.54)	39.3 (39.4)	96	1.55 (1.53)	39.3 (39.4)
			91	1.75 (1.73)	37.7 (39.4)

(b) 2D-type Potential ($V_2 < 0$)

$KC_{24}(H_2)_{0.5}$			$KC_{24}(H_2)_1$		
Barrier Height (meV)	ΔE_1 (meV)	ΔE_2 (meV)	Barrier Height (meV)	ΔE_1 (meV)	ΔE_2 (meV)
-49	29.2 (29.3)	10.7 (11.8)	-29	23.1 (23.7)	11.8 (11.8)
			-49	29.2 (29.3)	10.7 (11.8)

^{a} ΔE_1 refers to the $l, m(0, 0 \rightarrow 1, 0)$ transition.
^{b} ΔE_2 refers to the $l, m(0, 0 \rightarrow 1, \pm 1)$ transition.
^{c} Experimental peak positions are listed in parentheses.

ferent adsorption sites in KC_{24}. At the dilute $x = 0.25$ composition, the three distinct low-energy peaks originate from the dominant H_2-sorbent interaction, with little contribution from H_2-H_2 interactions. Each peak can be assigned to an adsorption site with a specific barrier to rotation. Simultaneous filling of these distinct sorption sites is indicated by the IINS data, as opposed to the preferential filling of the less-hindered sites.[4] In the $\left(\sqrt{7} \times \sqrt{7}\right) R\,19.11°$ structure used for the first-principles calculations, there is only one type of sorption site. As described in Sec. 2.3, though, the relaxed close-packed structure illustrated in Fig. 2.3b is the most compelling structure model for KC_{24}. For this structure there are a large number of sorption sites, each having a distinct crystal field symmetry. The filling of these sites would presumably produce multiple low-energy IINS peaks. However, many of these peaks may be experimentally indistinguishable due to the limited resolution

---

[4]Rotation barrier is not necessarily correlated to the adsorption enthalpy. It is not clear, therefore, whether the sites with a smaller rotational barrier would be energetically preferable.

of the spectrometer. The appearance of new peaks at large H_2 filling may indicate either the filling of energetically unfavorable sites, or the increasing contribution of H_2-H_2 interactions to the rotational potential.

Applying a simple hindered rotor model to a complex system has its limitations. For example, the model assumes a single, fixed adsorption site in an unchanging external crystal field, neglecting the effects of hydrogen-hydrogen interactions. The two-dimensional, anisotropic rotor model (with calculated rotational barriers) gives values that are clearly inconsistent with experiment. Furthermore, even the one-dimensional rotor model does not describe the intensities of observed peaks in a consistent manner. It pairs the weak 0.56 meV peak with the strong 52 meV peak, and pairs the strong 1.5 meV peak with the weak 39 meV peak. Moreover, it fails to explain the intermediate-energy spectral peaks between 10 meV and 30 meV. We can invoke a negative potential barrier of -29 meV which predicts transitions at 12 meV and 23 meV, in reasonable agreement with the observed data. From the first-principles calculations, however, there is no strong evidence for the existence of a negative rotational barrier in which the H_2 molecule tends to align parallel to the basal plane surface.

On the other hand, there is empirical evidence that the intermediate-energy peaks are somehow linked to the low-energy peaks. There is a strikingly similar pattern in the evolution of both the low-energy and intermediate-energy spectra as a function of H_2 filling. In the low-energy spectrum (see Fig. 6.4), Peak III begins to collapse at the $x = 1.5$ filling, while Peak IV increases sharply in intensity. In the intermediate-energy spectrum (see Fig. 6.6), Peak IV collapses at a concentration of $x = 1.5$ in conjunction with the rapid growth in Peak III. Based on this observation, a case can be made that the intermediate-energy peaks originate from multiple-excitations of both rotational and phonon modes. In

Sec. 6.5 the in-plane phonon transitions were estimated at around $8\,\mathrm{meV}$ (with an overtone at $26\,\mathrm{meV}$), and at $12\,\mathrm{meV}$ (with an overtone at $25\,\mathrm{meV}$). Therefore, a one-phonon + one-rotational excitation would be expected at $8 + 1 = 9\,\mathrm{meV}$ or $12 + 1 = 13\,\mathrm{meV}$, close to the observed peak at $12\,\mathrm{meV}$. Similarly, a two-phonon + one-rotational excitation would occur at $26 + 1 = 27\,\mathrm{meV}$, close to the experimental peak at $29\,\mathrm{meV}$. Multiple phonon-rotation excitations therefore help to explain the complex spectral features observed in the intermediate-energy-loss range. They also explain why the mass-scaling rules for pure phonon or rotational transitions are not observed. It should be recalled, however, that the phonons were calculated for a fixed H_2 orientation. In fact, the center-of-mass PE surface depends strongly on the molecular orientation, implying a strong translational-rotational coupling. Solving the phonon-rotation spectrum in such a situation is a complex problem. The presence of strong translational-rotational coupling may explain why we still observe large discrepancies between model and experiment for the IINS spectrum of $\mathrm{KC_{24}(H_2)}_x$.

6.7   Conclusion

A combination of IINS data and first-principles calculations have provided insights into the thermodynamics of H_2 adsorption in $\mathrm{KC_{24}}$. Evidence for multiple adsorption sites is present in the low-energy IINS spectra, particularly at the dilute $x = 0.25$ composition which probes the H_2-sorbent interactions. At more concentrated hydrogen compositions, the increasing H_2-H_2 interactions are reflected in the development of a fine-structure in the original three low-energy peaks. The one-dimensional hindered rotor model provides a reasonable description of the low-energy and high-energy IINS peaks, though further refinement of the rotational potential is needed. Dramatic changes in the low-energy spectra perhaps reflect a reconstruction of the potassium monolayer in response to large H_2 concen-

trations. Intermediate-energy spectral features are explained by multi-excitations of both phonon and vibrational modes. First principles calculations indicate strong coupling of the rotational and vibrational degrees of freedom for the adsorbed H_2 molecules.